International Journal of Heat and Mass Transfer 52 (2009) 3918–3928

Contents lists available at ScienceDirect

International Journal of Heat and Mass Transfer

journal homepage: www.elsevier.com/locate/ijhmt

Large-eddy simulation of mixed convection-radiation heat transfer in a vertical channel

Darioush G. Barhaghi, Lars Davidson *

Division of Fluid Dynamics, Department of Applied Mechanics, Chalmers University of Technology, SE-412 96 Göteborg, Sweden

ARTICLE INFO

Article history:
Received 6 January 2009
Accepted 23 March 2009
Available online 13 May 2009

Keywords:
Mixed convection boundary layer
Large-eddy simulation
LES
Radiation heat transfer

ABSTRACT

A mixed convection boundary layer in a vertical channel is studied using large-eddy simulation. Two different cases were considered by applying constant heat flux boundary condition to one of the channel walls while the other wall was kept insulated. The Grashof to Reynolds number ratios based on the wall heat flux and the channel width are $Gr_w/Re_w^2 = 9.4 \times 10^7/5080^2 = 3.6$ (Case I) and $2.5 \times 10^8/9575^2 = 2.8$ (Case II), which suggest that the buoyancy forces are comparable to the inertial forces in both cases. Owing to the large temperature differences between the hot wall and the inlet air, the governing equations were solved using two different approaches. Boussinesq approximation considering constant properties was employed in the first approach. In the other, fluid properties were assumed to be temperature dependent. A consequence of the wall high temperature is the radiation heat transfer, which is also taken into account. It is shown that an average of about 11% of the heat in Case I and 15% in Case II is transferred to the insulated wall via radiation. Differences between the results of the constant and variable property computations are rather high, which suggest that Boussinesq approximation is not accurate for very large temperature differences. The differences between the results of the variable and constant property computations are expectedly larger in Case II, where the wall temperature is higher than Case I. Large discrepancies can be observed between the numerical and experimental results. The discrepancies are larger in Case II than in Case I. The possible reasons for these discrepancies are discussed.

1. Introduction

Mixed convection heat transfer exists in a number of industrial applications where buoyancy forces are not negligible compared to inertial forces. The existence of the buoyancy forces can lead to impairment or enhancement of the heat transfer process depending on the direction of the flow, geometry configuration and the magnitude of the buoyancy forces. Buoyancy forces affect the mixing process by changing the production of turbulence in the region close to the wall, which has great influence on the turbulent flow regime in the vicinity of the wall (see e.g. [1–4]).

Natural convection boundary layer is studied experimentally in different geometries among which confined cavities with different aspect ratios, vertical and horizontal cylinders and vertical flat plates are the most common ones.

Natural convection boundary layer in a rectangular cavity filled with air and having an aspect ratio of five was studied in [5]. Since it was in practice difficult to establish a perfectly insulated boundary in the experiment, an asymmetric flow was reported. The reason was principally the imperfect insulation at the ceiling of the cavity where the heat loss, although very small, prohibited the flow from relaminarization. However, relaminarization at the floor of the cavity did take place. This geometry was studied by Barhaghi and Davidson [6] using LES method and different subgrid scale models. It was shown that the dynamic subgrid scale model was the most accurate model to capture the transition location, mean flow and turbulent parameters. It was also shown that the accuracy of the results in the transition region was highly grid dependent.

Low turbulence natural convection in an air filled square cavity was studied and the results for the thermal and fluid flow fields and turbulence quantities were published in [7] and [8], respectively. The experiments were conducted at a relatively low Rayleigh number $Ra = 1.58 \times 10^9$ and the contour plot of the thermal field and a vector plot of air flow in the cavity were reported for the first time. It is believed that in this experiment, the level of turbulence has been quite low, and the flow has been only transitional with a stratified quiescent flow in the core.

Betts and Bokhari [9] conducted an experiment in a cavity which was thin enough to make the flow in the core region fully turbulent. The experiment was performed at two different Rayleigh numbers, $Ra = 0.86 \times 10^6$ and $Ra = 1.43 \times 10^6$, based on the cavity width. The advantage of having a tall and thin cavity was that it made it easier to achieve two-dimensional results.

The budget of turbulence in the case of a natural convection boundary layer at four different Rayleigh numbers in an infinite,

* Corresponding author.
E-mail address: lada@chalmers.se (L. Davidson).

0017-9310/$ - see front matter Crown Copyright © 2009 Published by Elsevier Ltd. All rights reserved.
doi:10.1016/j.ijheatmasstransfer.2009.03.031

Nomenclature

Latin symbols

D_e	characteristic length, =2W
g	gravitational acceleration
k	thermal conductivity of air
P	pressure
$P_{u_iu_j}$	production term in the Reynolds stress equations
P_{u_it}	production term in the turbulent heat flux equations
P_{tt}	production term in the temperature variance equation
q''_w	wall heat flux
T	temperature, time period
T_b	bulk temperature, $= T_{in}$
T_f	film temperature, $(T_h[K] + T_c[K])/2$
T_h	hot wall local temperature
T_{in}	temperature of air at the inlet of the channel
t	time
Δt	computational time step
U	stream-wise direction velocity
U_b	bulk velocity
u^*	friction velocity, $\sqrt{(\nu \partial U/\partial y)}$
W	width of the channel
x	stream-wise coordinate
y	wall normal coordinate
z	span-wise coordinate
Δx^+	computational cell length in viscous units in the stream-wise direction
y^+	distance of the wall adjacent node from the channel wall in viscous units
Δz^+	computational cell length in viscous units in the span-wise direction

Greek symbols

β	coefficient of expansion, $1/T_f[K]$
ε	emissivity of the channel walls
ϕ	general variable
μ	dynamic viscosity of air
μ_{SGS}	turbulent SGS viscosity
ν	kinematic viscosity of air, μ/ρ
ρ	density of air

Dimensionless quantities

Gr_W	Grashof number, $g\beta q''_w W^4/\nu^2 k$
Re_W	Reynolds number, $U_b W/\nu$
Nu	local Nusselt number, $q''_w D_e/k(T_w - T_b)$
Pe	Peclet number, $\rho V/(\Gamma/\delta)$

differentially heated, vertical channel was studied by Versteegh and Nieuwstadt [10]. They observed that the velocity maximum moves towards the wall when the Rayleigh number is increased and the temperature gradient near the wall increases as well. It was also shown that the pressure strain correlation acts as a return-to-isotropy term in the middle of the channel, whereas this term provokes anisotropy near the wall.

Pure natural convection boundary layer on a vertical flat plate was studied experimentally in [4]. The results suggested that for values of y^+ between 20 and 100, $\overline{u}'v'$ is not correlated with the mean velocity gradient, $\partial U/\partial y$. Another unique feature of this flow was the production of turbulence in the region close to the wall which had large influence on the turbulent flow regime in the vicinity of the wall. In forced convection boundary layers, it is the Reynolds shear stress which contributes to the production of turbulence, whereas in natural convection boundary layer, it can be a sink term in the inner part of the boundary layer where the velocity gradient is positive. Consequently, the buoyancy production takes over the role of the source term and compensates for the production deficit due to the Reynolds shear stress. However, the results of the LES of natural convection boundary layer on a vertical cylinder in [2] did not completely comply with the findings of the mentioned experiment in the region close to the wall.

Turbulent natural convection around a heated vertical slender cylinder was studied in [11] and new turbulent structures were presented for the near wall region. It was shown that there exists a region of negative shear stress close to the cylinder contrary to the reported measurements in [4].

Four cases of a mixed convection boundary layer in the presence of radiation heat transfer were investigated in [12]. These cases include different heat flux and inlet mass flow rate boundary conditions. Both buoyancy aided and opposed configurations were studied for these cases. By comparing the results of the mixed convection with the pure forced convection boundary layer, it is shown, that in the cases of the buoyancy aided configuration, the Nusselt number is reduced when buoyancy forces are small. However, by gradually increasing the buoyancy forces, the Nusselt number increases and acquires higher values compared to the pure forced convection Nusselt number, suggesting that the turbulence and therefore the mixing process is considerably improved.

The buoyancy aided configuration of the third case in the above mentioned experiment was studied in [13] using large-eddy simulation. Because of large Peclet numbers in the computational cells, a blend of the central difference scheme and Van-Leer scheme was used to avoid spurious temperature and velocity fluctuations or the so called computational 'wiggles'. At the channel inlet, instantaneous DNS results of a fully developed channel were prescribed. However, it was shown that the scheme had dampened almost all resolved turbulent fluctuations near the inlet. This was speculated to be the reason for the large discrepancies between the experimental and numerical results.

In this work, by using a finer mesh, the authors are able to apply the pure central difference scheme to the velocities. The remaining discrepancies between the numerical and experimental results are discussed. Another interesting aspect is the way the boundary layer evolves along the vertical channel, which is absent in the experimental results. The physics behind this behavior is explained in the present work.

2. Geometry and boundary conditions

Fig. 1 represents the buoyancy aided channel flow configuration used in [12]. The channel left wall is kept insulated for $x > 1$ m. For $x < 1$ m, the temperature of the walls is equal to the surrounding temperature. At the right wall, a constant heat flux boundary condition is applied. The heat fluxes applied for $x > 1$ m are $q''_w = 449\ \mathrm{W/m^2}$ and $1502\ \mathrm{W/m^2}$, respectively, for the two cases considered. In the former case, hereafter Case I, the inlet air temperature and Reynolds number are T_{in}=18.6 °C and $Re_W = 5080$, respectively, while in the latter case, hereafter Case II, they are $T_{in} = 20.2\ ^\circ C$ and $Re_W = 9575$. The Grashof number for the two cases are $Gr_W = 9.4 \times 10^7$ and $Gr_W = 2.5 \times 10^8$, respectively.

The velocity components of the instantaneous DNS results of a fully developed channel are prescribed as the inlet boundary condition. At the outlet, a convective boundary condition is used for the velocities and temperature. A cyclic boundary condition is applied to all of the parameters in the span-wise (z) direction.

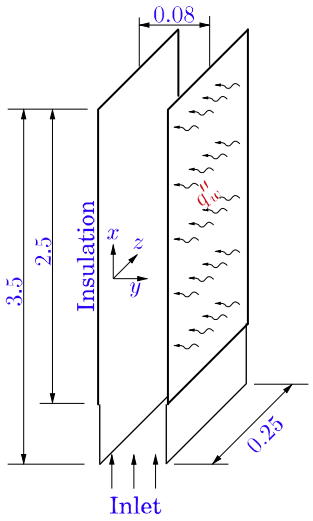

Fig. 1. Computational domain. All dimensions are in meters.

Owing to the high temperature of the hot wall, the radiation heat transfer is significant in both cases. The radiation heat transfer is assumed to be two-dimensional, assuming that the span-wise variation of the temperature is negligible. The emissivity of the channel walls is assumed to be $\varepsilon = 0.125$ (according to [12]) and the inlet and outlet are assumed to be black body surfaces.

3. Grid

The grid size for Case I with the lower Reynolds number is $482 \times 66 \times 66$ in the x, y and z directions, respectively. In Case II, with the higher Reynolds number, the grid resolution is $578 \times 98 \times 98$. The grids are equidistant in the streamwise and spanwise directions and a 9% stretch factor is used in the wall-normal (y) direction.

The spatial resolution of the grid in Case I along the hot wall is $\Delta z^+ < 33$ and $\Delta x^+ < 50$ in the span-wise and stream-wise directions, respectively. The grid in Case II has the resolutions of $\Delta z^+ < 20$ and $\Delta x^+ < 50$.

4. Numerical method

Applying a constant heat flux boundary condition at the hot wall causes the temperature of the hot wall to rise in the streamwise direction. In the primary RANS computations, it was found that the temperature differences between the hot wall and inlet air were as high as 100 °C and 220 °C in the two cases, respectively. The first consequence of the large temperature difference in the flow is the ambiguity of the Boussinesq approximation validity. It was shown in [14] that even for moderate Rayleigh numbers, the non-Boussinesq conditions have severe effect on the Nusselt number distribution in case of natural convection in a Rayleigh–Bénard system. Thus, the Navier–Stokes and the energy equations are not only solved using Boussinesq approximation but are solved by also considering variable density, viscosity, conductivity and specific heat. All these properties are extracted from the thermodynamical tables, and fourth-order polynomial equations are fitted to them assuming the properties are independent of the pressure.

4.1. Finite volume approach

A conventional finite volume method (see [15]) is used to solve the three-dimensional continuity, Navier–Stokes and temperature equations. Implicit spatial filtering is applied to the equations with constant properties. However, Favre averaged equations are solved in the case with the variable properties. The dynamic subgrid-scale model of [16] is used to model the small eddies. Details on the implementation can be found in [17] and [6]. The second-order Crank–Nicolson scheme is used to discretize all the equations in time. A blend of the central difference scheme with deferred correction (see [18]) and Van-Leer scheme in conjunction with a 'wiggle' detector is used to discretize the temperature equation in space. However, the pure central difference scheme is used to discretize the velocity equations. It was found in [13] that the blended scheme between central differencing and a second-order bounded scheme destroyed nearly all resolved fluctuations in the inlet region. The suppression of the resolved turbulence fluctuations is a consequent of the fact that it is almost impossible to differentiate between the turbulence fluctuations and the spurious ones in the case of the velocities. Thus, the scheme may incorrectly dissipate turbulence fluctuations instead of the spurious fluctuations. Fortunately, in the case of the temperature, it is easy to recognize a 'wiggle'. A 'wiggle' in this case is defined to be the local minima or maxima or when the temperature in a cell is higher or lower than the maximum or minimum boundary values (inlet and walls). Pure central differencing is used for the velocity. This was possible since the mesh is finer than that used in [13].

The numerical procedure is based on an implicit, fractional step technique with a multi-grid pressure Poisson solver and a non-staggered grid arrangement. The pressure Poisson equation in the case of the constant property equations reads:

$$\frac{\partial^2 P}{\partial x_i \partial x_i} = \frac{\rho}{\Delta t}\frac{\partial u_i^*}{\partial x_i} \tag{1}$$

where u_i^* is the intermediate velocity in the fractional step solution procedure (see [19] for details). In the variable property case, considering the continuity equation, the Poisson equation for pressure reads:

$$\frac{\partial^2 P}{\partial x_i \partial x_i} = \frac{1}{\Delta t}\left(\frac{\partial \rho}{\partial t} + \frac{\partial \rho u_i^*}{\partial x_i}\right) \tag{2}$$

4.2. Radiation heat transfer

Since the temperature of the heated wall increases considerably, the radiation heat transfer comes into effect. The radiation heat transfer is assumed to be two-dimensional, and the span-wise variation of the radiation is neglected. Fig. 2 shows a schematic diagram of the vertical channel where its walls are segmented by two-dimensional strips (for more information on the network approach refer to [20]). In this figure, l and r stand for the left and

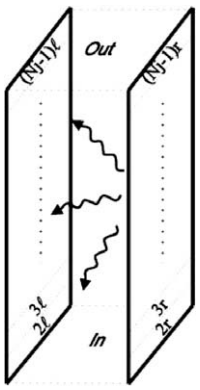

Fig. 2. Schematic diagram of the radiation heat transfer in the channel.

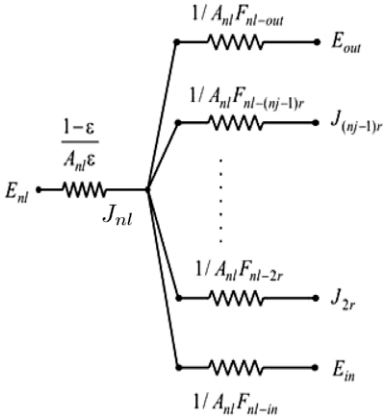

Fig. 3. Equivalent circuit diagram of the radiation heat transfer in the channel.

right walls, respectively, and $nj-1$ is the number of cells in the stream-wise direction.

The equivalent circuit diagram of the radiation exchange between the nth strip on the left wall ($n=2\ldots nj-1$), the right wall strips, the inlet and outlet is shown in Fig. 3. The inlet and the outlet are assumed to be black bodies, and the area weighted average temperature at the outlet is assumed to be that of the fluid.

By considering this diagram for the left or insulated wall and a similar diagram for the right or heated wall, the governing equations for the left and right segment radiosities, J_{nl} and J_{nr}, read:

$$J_{nl}\left(\frac{1}{1-\varepsilon}\right)-\sum_{m=2}^{nj-1}(J_{mr}F_{nl-mr})=E_{nl}\left(\frac{\varepsilon}{1-\varepsilon}\right)+E_{out}F_{nl-out}+E_{in}F_{nl-in} \quad (3)$$

$$J_{nr}\left(\frac{1}{1-\varepsilon}\right)-\sum_{m=2}^{nj-1}(J_{ml}F_{nr-ml})=E_{nr}\left(\frac{\varepsilon}{1-\varepsilon}\right)+E_{out}F_{nr-out}+E_{in}F_{nr-in} \quad (4)$$

in which F_{nl-mr} is the view factor between the nth segment on the left wall and mth segment on the right or heated wall, $\varepsilon=0.125$ is the emissivity of the walls and E is the black body emission of a segment where the name of the segment is written as the subscript.

With regard to Fig. 4, view factors between the channel wall segments (considering two dimensionality) are calculated by Eqs. 5 and 6.

$$\begin{cases} F_{r-l}=\frac{\sqrt{(n+1)^2A^2+1}-2\sqrt{n^2A^2+1}+\sqrt{(n-1)^2A^2+1}}{2A} \\ A=H/W, n=|x_r-x_l|/H \end{cases} \quad (5)$$

$$\begin{cases} F_{r-l}=\frac{W}{H}\left[\left(\frac{A-\sqrt{1+A^2}}{2}\right)-\left(\frac{A'-\sqrt{1+A'^2}}{2}\right)\right] \\ A=h/W, A'=(h-H)/W \end{cases} \quad (6)$$

Eqs. (3) and (4) are composed of $2\times(nj-1)$ equations that are solved by a Gauss–Seidel method at each time step. Provided the radiosities, the radiated and irradiated heat flux at each time step can be calculated using Eq. (7).

$$\begin{cases} q''^{irrad}_{nl}=\frac{E_{nl}-J_{nl}}{(1-\varepsilon)/\varepsilon} \\ q''^{rad}_{nr}=\frac{E_{nr}-J_{nr}}{(1-\varepsilon)/\varepsilon} \end{cases} \quad (7)$$

The irradiated heat flux will be used as the actual heat flux of the left wall (instead of the zero value corresponding to the insulated wall) and the radiated heat flux will be subtracted from q'_w to account for the effect of the radiation heat transfer.

5. Results

Sampling is started after assessing fully developed flow condition by tracking the time variation of the instantaneous Nusselt number at different heights. In the constant property case, time-averaged results are calculated. Considering instantaneous param-

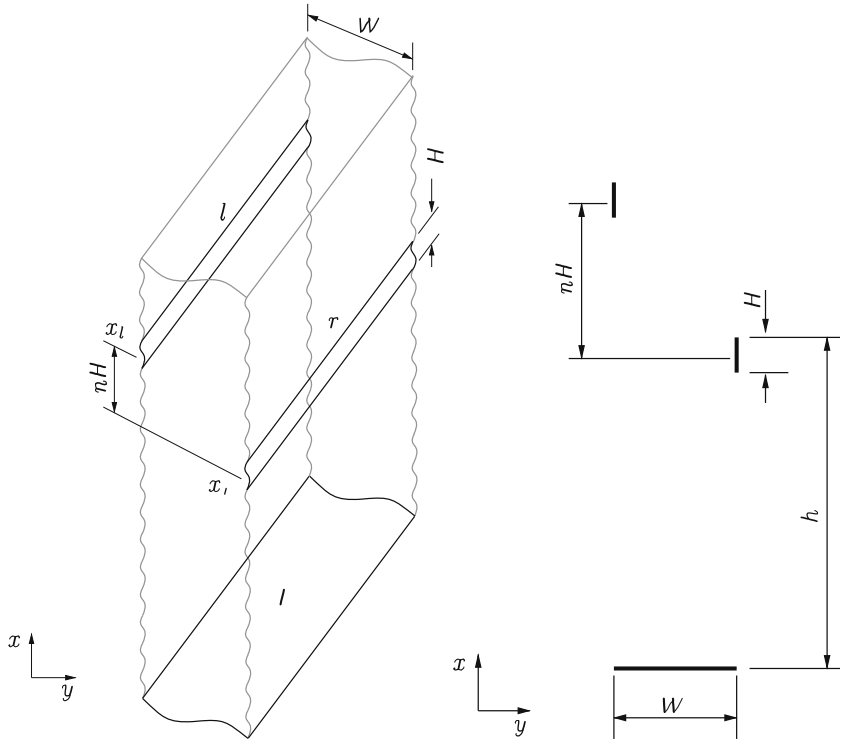

(a) Three-dimensional configuration. (b) Two-dimensional configuration.

Fig. 4. The geometrical dimensions that are used to calculate the view factors (see Eqs. (5) and (6)).

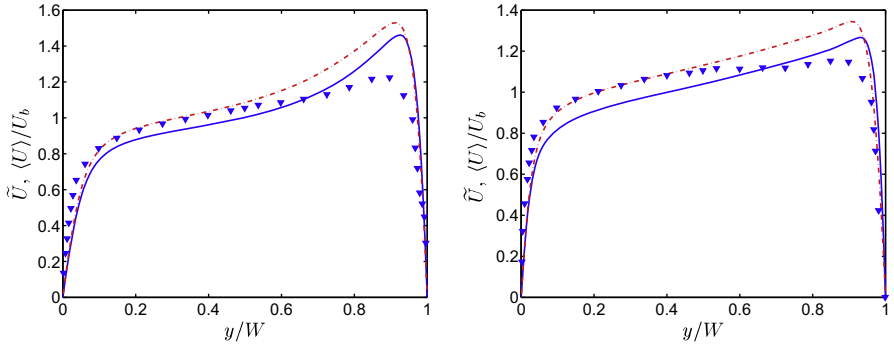

(a) Case I, $Gr_w/Re_w^2 = 3.6$. (b) Case II, $Gr_w/Re_w^2 = 2.8$.

Fig. 5. Averaged velocity profiles at $x = 3$ m. —: constant property computations; –·–: variable property computations; ▽: experimental results of [12].

eter ϕ, time averaged $\langle\phi\rangle$ in the period of time T is defined as $\langle\phi\rangle = 1/T\int_0^T \phi dt$. In the variable property case, however, a Favre averaging definition is used to calculate the averaged results. Favre averaged $\widetilde{\phi}$, considering time averaging definition, is defined as $\widetilde{\phi} = \langle\rho\phi\rangle/\langle\rho\rangle$. In the following, unless otherwise stated, the results of the case with the variable properties including radiation are presented.

5.1. Mean flow parameters

Fig. 5 compares the velocities obtained by the constant and variable property computations for the two cases. The reference velocities are the bulk velocities at the inlet, which are $U_b \approx 0.95$ and 1.8 m/s for Case I and Case II, respectively. In both cases, the variable property results are closer to the experimental results near the insulated wall. However, the discrepancies between the numerical and experimental results are larger close to the hot wall. The differences are greatest in Case I. Since the density is constant in the constant property computations, the bulk velocities and therefore the reference velocities remain constant along the channel. However, in the variable property case, the density decreases as the temperature of the air increases along the channel. Consequently, due to the conservation of mass, the bulk velocities have to increase along the channel in the variable property cases. Using local bulk velocities for the variable property cases, it is shown in Fig. 6 that the differences between the results are almost negligible.

Radiation is calculated at each time step and is added as a sink/source term to the cells adjacent to the hot/insulated wall. Fig. 7 shows the averaged wall heat flux on the hot wall. It can be seen that the radiation heat transfer increases as the temperature of the wall increases in both cases. As expected, the radiation heat transfer is almost independent of the fluid properties since it is assumed that the fluid is fully transparent with zero absorptivity.

In the computations, the outlet is assumed to be a black body surface with a temperature equal to the mass flow averaged temperature of the air at the outlet. This is the reason why the heat flux decreases steeply near the outlet. On average, about 11% of the heat flux in Case I and 15% of that in Case II is transferred to the insulated wall via radiation.

Nusselt number variations along the hot wall in the two cases are compared with the experimental results in Fig. 8. In Case I, the results of the constant and variable property computations are in reasonably good agreement with the measurements. However, in Case II, the differences are too large, especially in the case of the variable property computations. Surprisingly, the measured Nusselt number at the beginning of the channel is much larger than the predicted results. The temperature of the wall at this part of the channel is still low meaning that the amount of radiation heat transfer is also small. This can be understood in Fig. 7. Such a high Nusselt number at the beginning of the channel suggests that the measured wall temperature is much lower than the computed one since $T_w = q''_w D_e/Nu\ k + T_b$. This indicates that a considerable part of the heat is lost in the very beginning of the channel to the surroundings in the experimental rig.

The heat loss in the beginning of the channel explains why the predicted velocities near the hot wall in Fig. 5 are larger than the measured velocity. This can be investigated by considering the conservation of energy. Assuming no heat loss, $Q_{in} = Q_{out}$. In other words, $T_{b,out} = q''_w A_w/\dot{m}_{in}c_p + T_{b,in}$. Knowing that the bulk velocity and temperature at the inlet in Case II are 1.83 m/s and 20.2 °C, respectively, the bulk temperature can be calculated at the location at which velocity is measured. By employing the conservation of

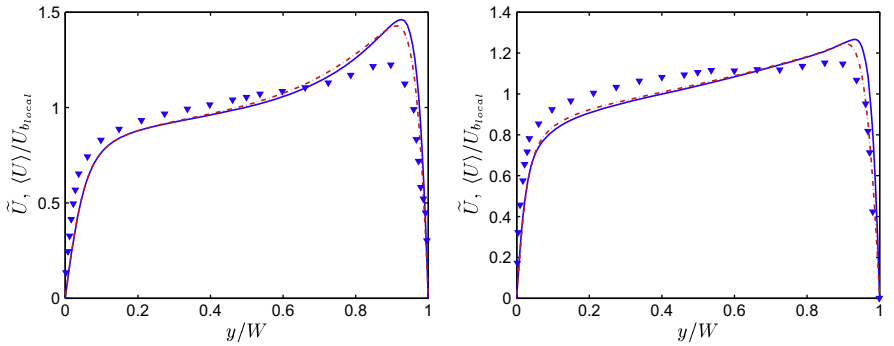

(a) Case I. (b) Case II.

Fig. 6. Averaged velocity profiles at $x = 3$ m. Local bulk velocities are used as the reference velocities. —: constant property computations; –·–: variable property computations; ▽: experimental results of [12].

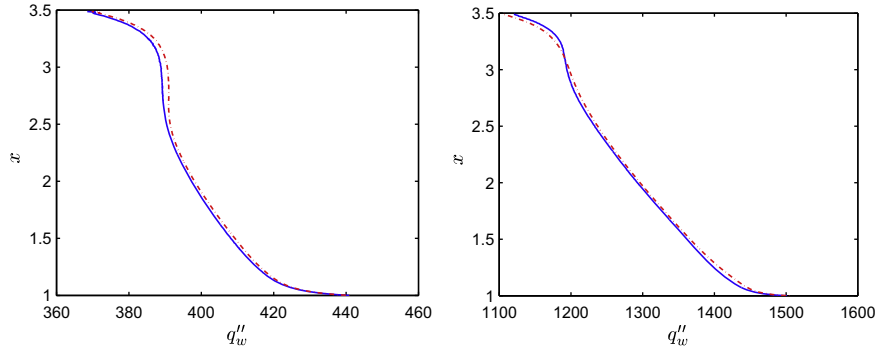

(a) Case I, $q''_w = 449\ W/m^2$. (b) Case II, $q''_w = 1502\ W/m^2$.

Fig. 7. Effect of radiation heat transfer on the hot wall heat flux distribution. —: constant property computations; –·–: variable property computations.

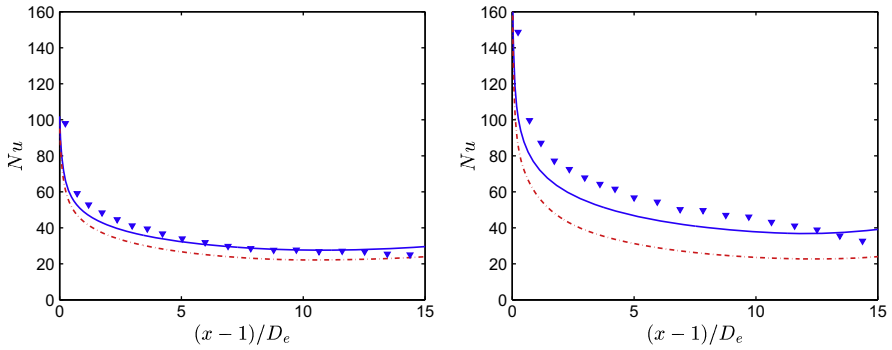

(a) Case I. (b) Case II.

Fig. 8. Nusselt number variations along the hot wall. —: constant property computations; –·–: variable property computations; ▽: experimental results of [12].

mass, the calculated bulk velocity at $x = 3$ m is 1.93 m/s, which is in very good agreement with the LES computations.

The effect of the radiation on the calculated temperature of the insulated wall in the variable property computations can be seen in Fig. 9. Because of higher temperature differences between the hot wall and the inlet temperature in Case II (see Fig. 9), it may be expected that the deviation of the variable property results from the Boussinesq approximation would be larger in this case. This behavior can be observed by comparing Figs. 8a and b. This is however mainly caused by the differences between the air conductivity in the two cases.

5.2. Turbulence parameters

Turbulent Reynolds shear stresses in the two cases are compared with the experimental results in Fig. 10. Like the mean flow results, the discrepancies between the computations and measurements are large near the hot wall, where the magnitude of the measured shear stresses is much smaller than that of the predicted ones.

With regard to the predicted shear stresses, the largest differences between the variable and constant property simulations occur in the middle of the channel. This is probably due to the fact that the density differences play a more important role in this region. The magnitude of the variable property shear stress is also in Fig. 10a higher than the constant property shear stress, while the reverse is true in Fig. 10b. The reason may be the normalization of the shear stresses by the inlet bulk velocity, which is not an appropriate variable. A more suitable parameter would be the friction velocity.

Fig. 11 compares the normal Reynolds stresses with the experimental results. Similar to the turbulent shear stress, discrepancies

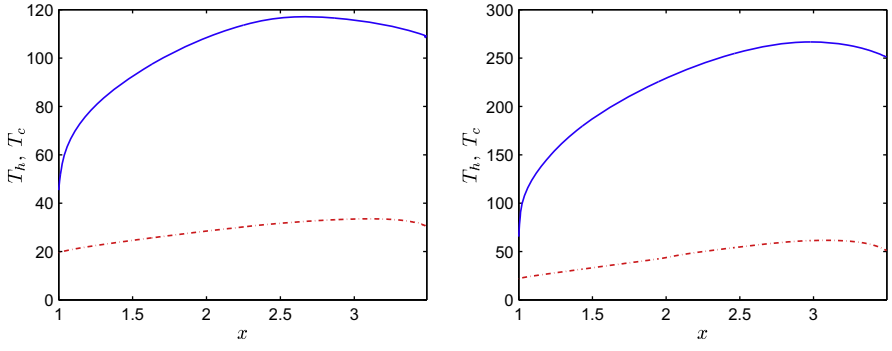

(a) Case I. (b) Case II.

Fig. 9. Temperature variations along the channel walls. —: hot wall temperature; –·–: insulated wall temperature.

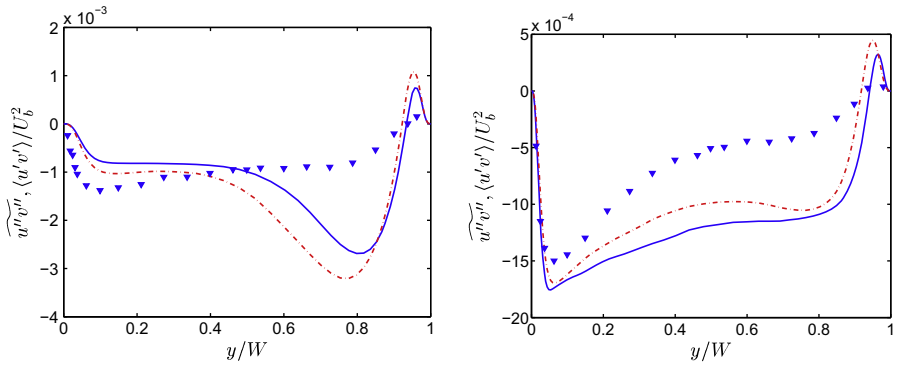

(a) Case I. (b) Case II.

Fig. 10. Reynolds shear stress comparison at $x = 3$ m. —: constant property computations; –·–: variable property computations; ▽: experimental results of [12].

between the computations and measurements are large near the hot wall. The measured turbulence intensity near the hot wall is smaller than the predicted one. Nevertheless, both computations and experiments confirm that the turbulence intensity in Case I is larger than that in Case II, although both the Grashof and the Reynolds numbers are higher in Case II.

Two local maxima near the hot wall can be recognized in examining the computed $\widetilde{u''u''}$. The local minimum between the two maxima lies close to the location at which the velocity is maximum or the shear stress is zero. At this point, it is the streamwise turbulent heat flux, $\widetilde{u''t''}$, that contributes to the production of $\widetilde{u''u''}$. This behavior can be seen in Fig. 12, which compares the production of $\widetilde{u''u''}$ in both cases. Comparing the production caused by the shear stress, P_{11}, in the vicinity of the hot wall, it can be seen how much larger this term is in Case I than in Case II. The larger production near the hot wall in Case I explains why the normal Reynolds stresses in this region are larger in Case I than in Case II (see Fig. 11).

The turbulent heat fluxes, $\widetilde{u''t''}$ and $\widetilde{v''t''}$, and the temperature fluctuations, $\widetilde{t''t''}$, are shown in Fig. 13 for the two cases. While the behavior of these parameters is similar in both cases, the magnitudes of $\widetilde{u''t''}$ and $\widetilde{t''t''}$ are larger in Case II than in Case I. No experimental results are available for comparison with these calculated parameters.

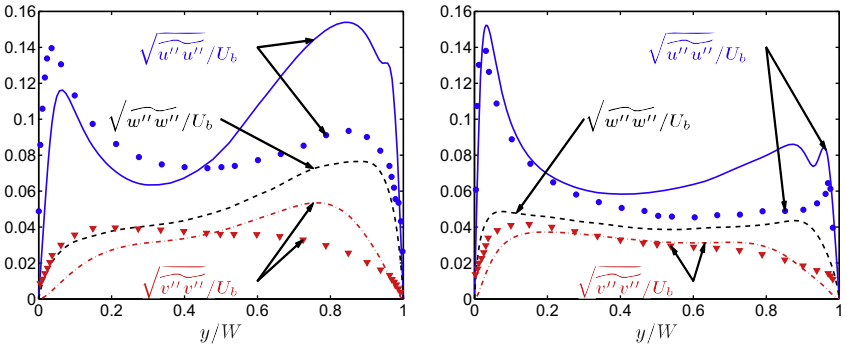

(a) Case I. (b) Case II.

Fig. 11. Comparison of the normal Reynolds stresses with the experimental results at $x = 3$ m. Lines: results of the variable property computations; markers: experimental results of [12].

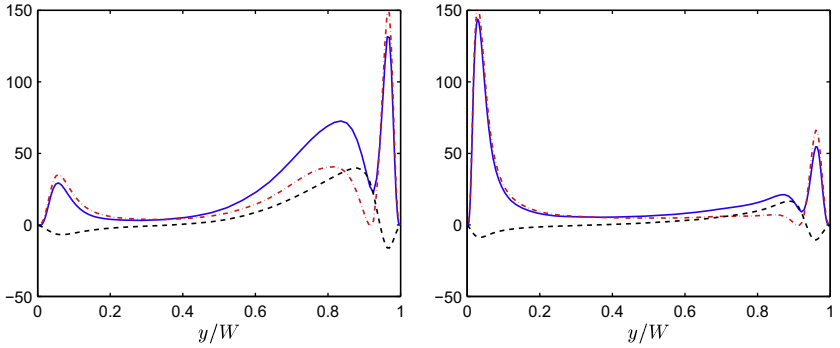

(a) Case I. (b) Case II.

Fig. 12. Production of the streamwise normal stress, $P_{uu} = P_{11} + G_{11} = -2\widetilde{u''v''}\partial\tilde{U}/\partial y + 2g\beta\widetilde{u''t''}$. All terms are normalized by u^{*3}. —: $P_{11} + G_{11}$; –·–: $P_{11} = -2\widetilde{u''v''}\partial\tilde{U}/\partial y$; – – –: $G_{11} = 2g\beta\widetilde{u''t''}$.

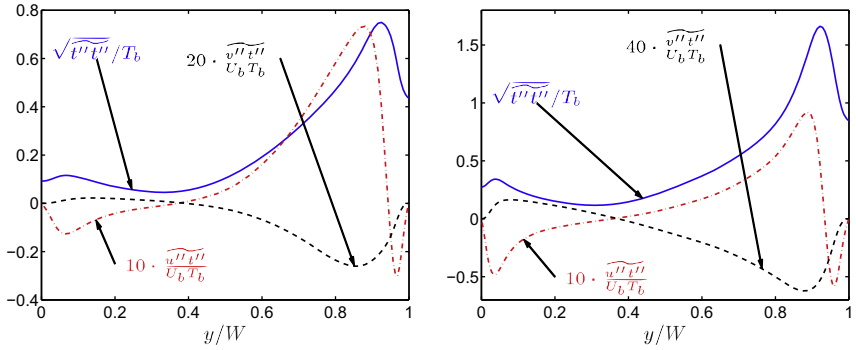

(a) Case I. (b) Case II.

Fig. 13. Turbulent heat fluxes and temperature fluctuations at $x = 3$ *m*. Lines: results of the variable property computations.

5.3. Effect of radiation heat transfer

The effect of neglecting or increasing the radiated heat transfer on the velocity and turbulent shear stress is investigated in this section.

Fig. 14 compares the velocity and shear stress results of the constant property computations of Case I with the case in which the radiation is neglected. It can be seen that by neglecting the radiation, velocity is slightly increased near the hot wall since more heat is transferred to the fluid in this region. Consequently, the density is underestimated (or the buoyancy term that is estimated by the Boussinesq approximation is overestimated) which results in velocity increase near the hot wall. The impact of neglecting the radiation is considerably larger on the region close to the insulated wall. This can be observed in Fig. 14b where the turbulent shear stresses are compared. Removing the irradiated heat transfer from the insulated wall, destroys the existing buoyancy force which in turn reduces the impairment of the turbulent shear stress level in this region.

Increase of the irradiated heat transfer to the insulated wall by doubling the emissivity of the walls in Case II is also investigated and the results are shown in Fig. 15. Although this has little influence on the velocity profile (Fig. 15a), the effect is substantially larger on the turbulent shear stress near the insulated wall. Larger

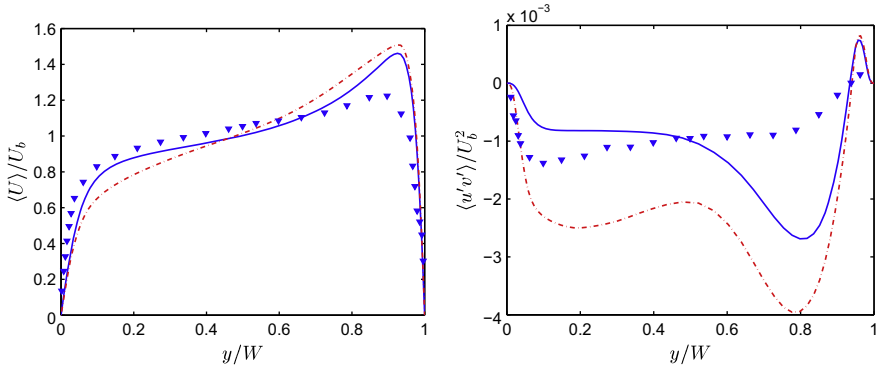

(a) Velocity profiles. (b) Shear stress profiles.

Fig. 14. Effect of radiation heat transfer on the velocity and shear stress. Fluid properties are constant in both cases. —: Case I with radiation heat transfer; –·–: Case I with neglected radiation heat transfer; ▽: measurements of [12].

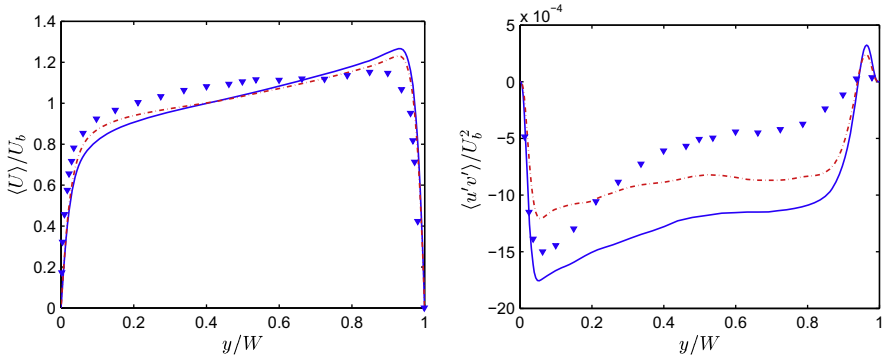

(a) Velocity profiles. (b) Shear stress profiles.

Fig. 15. Effect of increased radiation heat transfer on the velocity and shear stress. Fluid properties are constant in both cases. —: Case II with $\varepsilon = 0.125$; –·–: Case II with $\varepsilon = 0.250$; ▽: measurements of [12].

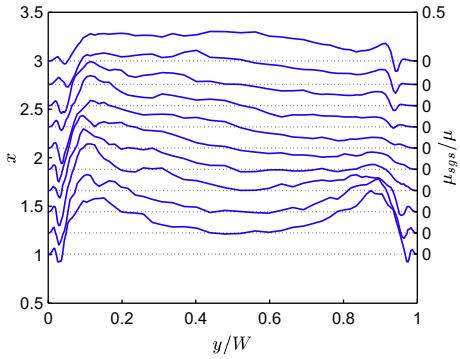

Fig. 16. $\langle \mu_{sgs} \rangle$ profiles across the channel at different heights.

irradiation, results in larger buoyancy force which in turn increases the impairment of the turbulence by reducing the magnitude of the shear stress.

6. Boundary layer development

In this section, the boundary layer development is studied by investigating the behavior of the mean flow and turbulent parameters of Case I at different heights of the vertical channel.

The calculated SGS-viscosity at different heights of the channel is shown in Fig. 16. It can be seen that the SGS-viscosity has acquired negative values in small regions close to the hot wall for $x > 1.75$ m. In these regions where the energy cascade is reversed, the SGS model reduces the viscous diffusion.

The development of the velocity and temperature profiles along the channel is shown in Fig. 17. It can be seen in Fig. 17a that the fluid acquires higher velocity magnitudes close to the hot wall as it moves downstream. Temperature profiles also show that the boundary layer becomes thicker as it develops in the channel passage.

Two important parameters that play an essential role in the development of turbulent boundary layer are the turbulent shear stress ($\widetilde{u''v''}$) and the wall normal turbulent heat flux ($\widetilde{v''t''}$), which are shown in Fig. 18.

At $x = 1$ m, where the heat flux boundary condition is applied, a symmetrical profile of a fully developed channel flow can be observed in the case of the turbulent shear stress. Since the temperature boundary layer is just forming, $\widetilde{v''t''}$ is zero at this height. Near the hot wall, as the boundary layer grows, $\widetilde{u''v''}$ is reduced. As the flow goes upward, $\widetilde{u''v''}$ in the inner part of the boundary layer ($y/W > 0.9$), eventually becomes zero, from which it again starts to attain positive values. However, in the outer part of the boundary layer, ($0.5 < y/W < 0.9$), the negative shear stress attains larger magnitudes since the production of shear stress, $P_{uv} = -\widetilde{v''v''}\partial\tilde{U}/\partial y + g\beta\widetilde{v''t''}$, is negative (due to a positive velocity gradient and negative wall normal heat flux). However, in the inner part of the boundary layer, the production of shear stress due to $\widetilde{v''v''}$ is larger than the negative heat flux term, resulting in positive shear stress in the inner boundary layer.

Considering the major production term of the wall normal turbulent heat flux, $P_{vt} = -\widetilde{v''v''}\partial\tilde{T}/\partial y$, it can be concluded that, due

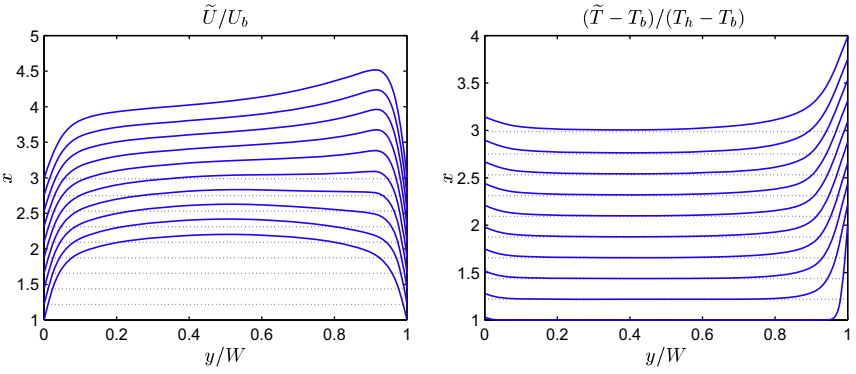

(a) Velocity profiles. (b) Temperature profiles.

Fig. 17. Velocity and temperature profiles across the channel at different heights.

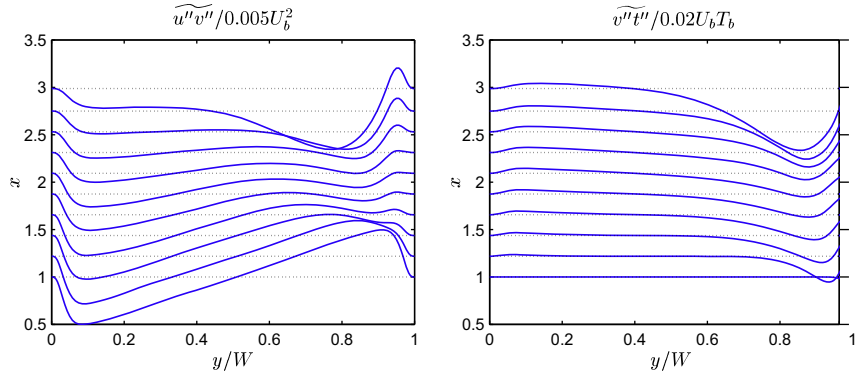

(a) Turbulent shear stress. (b) Wall normal turbulent heat flux.

Fig. 18. $\widetilde{u''v''}$ and $\widetilde{v''t''}$ profiles across the channel at different heights.

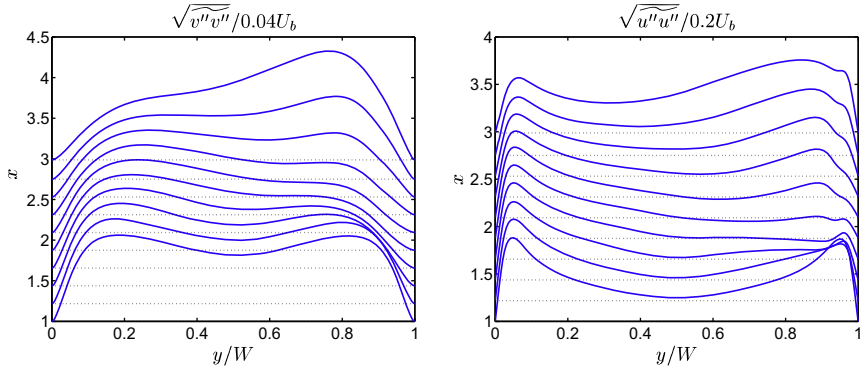

(a) Wall normal Reynolds stress. (b) Stream-wise Reynolds stress.

Fig. 19. $\widetilde{v''v''}$ and $\widetilde{u''u''}$ profiles across the channel at different heights.

to the positive temperature gradient and consequently negative P_{vt}, $\widetilde{v''t''}$ attains negative values close to the hot wall.

Since $\widetilde{v''v''}$ plays an important role in the productions of $\widetilde{u''v''}$ and $\widetilde{v''t''}$, its development as the boundary layer grows is shown in Fig. 19. $\widetilde{v''v''}$ is symmetrical at the location at which the temperature boundary layer begins. As the boundary layer evolves, $\widetilde{v''v''}$ attains in the first half of the channel larger/smaller values close to the insulated/hot wall, but the situation is reversed towards the end of the channel and $\widetilde{v''v''}$ becomes larger near the hot wall than near the insulated wall.

The Reynolds shear stress together with the stream-wise turbulent heat flux have significant impacts on $\widetilde{u''u''}$, whose variations across the channel at different heights are shown in Fig. 19. This can be understood by considering the production of $\widetilde{u''u''}$, whose major terms are $-2\widetilde{u''v''}\partial\tilde{U}/\partial y$ and $2g\beta\widetilde{u''t''}$. In the inner boundary layer at the hot wall, owing to the negative velocity gradient and positive shear stress, the former term is positive. However, the latter term is negative due to the negative $\widetilde{u''t''}$ (see Fig. 20a). Nevertheless, as the magnitude of the production caused by the shear stress is larger, the total production remains positive. In the outer boundary layer, where $\widetilde{u''v''}$ and $\widetilde{v''t''}$ are negative, and $\widetilde{t''t''}$, the velocity and temperature gradients are positive, $P_{ut} = -\widetilde{v''t''}\partial\tilde{U}/\partial y - \widetilde{u''v''}\partial\tilde{T}/\partial y + g\beta\widetilde{t''t''}$ remains positive, which results in a positive $\widetilde{u''t''}$. Consequently, in the outer layer, the positive and large $\widetilde{u''t''}$ makes the $\widetilde{u''u''}$ large in the boundary layer.

Fig. 20b shows the trend of $\widetilde{t''t''}$ at different heights of the channel. It can be seen that, as the boundary layer along the hot wall grows, $\widetilde{t''t''}$ attains larger values owing to the negative $\widetilde{v''t''}$ and positive temperature gradient, which makes its production, $P_{tt} = -2\widetilde{v''t''}\partial\tilde{T}/\partial y$, remain positive and increase along the channel as $|\widetilde{v''t''}|$ increases.

In turn, $\widetilde{t''t''}$, $\widetilde{v''t''}$ and $\widetilde{u''v''}$ affect the stream-wise turbulent heat flux. Positive $\widetilde{u''v''}$ results in a negative $\widetilde{u''t''}$ in a small region close to the hot wall, as P_{ut} is negative in that region. However, beyond this region, as the turbulent shear stress changes sign, $\widetilde{u''t''}$ attains positive values in a major portion of the boundary layer.

7. Conclusions

The boundary layer development in a vertical channel is studied using large-eddy simulation. A dynamic model is used as the SGS model. This model has captured the backscattered energy in the regions close to the hot wall where the SGS-viscosity has acquired negative values.

A so called 'wiggles' detector scheme is used but is applied only to the temperature because it was found in [13] that the use of this scheme for velocities had dampened the prescribed turbulence at the inlet.

In the two different cases that are studied in this work, radiation heat transfer has to be taken into account since the temperature of the hot wall is relatively high. The effect of the radiation on the mean flow and turbulence parameters is shown to be important.

Owing to relatively high temperature differences, the full governing equations with variable properties are solved. The Boussinesq approximation yields reasonable results, even for temperature differences as high as 220 °C (although it should be mentioned that the film temperature of the flow does not change more than 30 °C). The largest differences between the variable and constant property results occur in the middle of the channel. Nevertheless, even full equations result in considerably different mean flow and turbulence parameters compared to the measurements. The accuracy of the radiation heat transfer model is unlikely

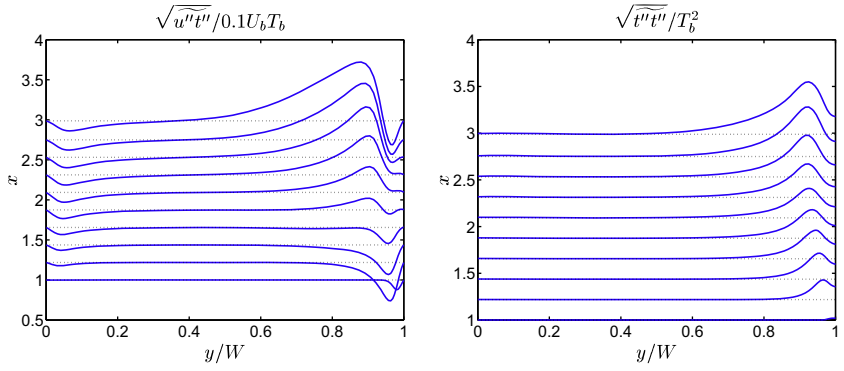

(a) Stream-wise turbulent heat flux. (b) Temperature fluctuations.

Fig. 20. $\widetilde{u''t''}$ and $\widetilde{t''t''}$ profiles across the channel at different heights.

to be the reason for this discrepancy since even doubling the emissivity of the walls does not considerably change the behavior of the mean flow and turbulence near the hot wall significantly.

A comparison of the computed and measured results shows that the measured profiles at $x = 3.0$ m are more similar to the computed profiles at lower heights, i.e. the computed profiles at $2.0\text{ m} \leqslant x \leqslant 2.5$ m. This suggests that the boundary layer in the experimental case has developed more slowly than in the computations. It is likely that the heat loss from the hot wall has resulted in this difference. By comparing the measured and computed results, it is shown that the major heat loss has occurred in the regions close to the very first heaters ($x = 1$ m). This is expected since no thermal insulation is used in the lower part of the channel ($x < 1$ m). Some part of the heat is consequently conducted to the lower part of the channel wall where it is convected to the surroundings.

References

[1] L. Davidson, D. Čuturić, S.-H. Peng, DNS in a plane vertical channel with and without buoyancy, in: K. Hanjalić, Y. Nagano, M.J. Tummers (Eds.), Turbulence Heat and Mass Transfer, vol. 4, (Begell House, New York, 2003), pp 401–408.

[2] D.G. Barhaghi, L. Davidson, R. Karlsson, Large-eddy simulation of natural convection boundary layer on a vertical cylinder, Int. J. Heat Fluid Flow 27 (2006) 811–820.

[3] T. Tsuji, Y. Nagano, Characteristics of a turbulent natural convection boundary layer along a vertical flat plate, Int. J. Heat Mass Transfer 31 (8) (1988) 1723–1734.

[4] T. Tsuji, Y. Nagano, Turbulence measurements in a natural convection boundary layer along a vertical flat plate, Int. J. Heat Mass Transfer 31 (10) (1988) 2101–2111.

[5] R. Cheesewright, K.J. King, S. Ziai. Experimental data for the validation of computer codes for the prediction of two-dimensional buoyant cavity flows, in: International symposium on cavitation and multiphase flow, ASME Winter Annual Meeting, HTD-60, Anaheim, 1986, pp. 75–81.

[6] D.G. Barhaghi, L. Davidson, Natural convection boundary layer in a 5:1 cavity, Phys. Fluids 19 (2007) 125106.

[7] Y.S. Tian, T.G. Karayiannis, Low turbulence natural convection in an air filled square cavity. Part I: The thermal and fluid flow fields, Int. J. Heat Mass Transfer 43 (2000) 849–866.

[8] Y.S. Tian, T.G. Karayiannis, Low turbulence natural convection in an air filled square cavity. Part II: The turbulence quantities, Int. J. Heat Mass Transfer 43 (2000) 867–884.

[9] P.L. Betts, I.H. Bokhari, Experiments on turbulent natural convection in an enclosed tall cavity, Int. J. Heat Fluid Flow 21 (6) (2000) 675–683.

[10] T.A.M. Versteegh, F.T.M. Nieuwstadt, Turbulent budgets of natural convection in an infinite, differentially heated, vertical channel, Int. J. Heat Fluid Flow 19 (1998) 135–149.

[11] N.J. Persson, R.I. Karlsson, Turbulent natural convection around a heated vertical slender cylinder, in: 8th International Symposium on Applications of Laser Techniques to Fluid Mechanics, Lisbon, 1996.

[12] J. Wang, J. Li, J.D. Jackson, A study of the influence of buoyancy on turbulent flow in a vertical plane passage, Int. J. Heat Fluid Flow 25 (2004) 420–430.

[13] D.G. Barhaghi, L. Davidson, LES of mixed convection boundary layer between radiating parallel plates, in: K. Hanjalić, Y. Nagano, S. Jakirlić (Eds.), Turbulence, Heat and Mass Transfer 5, Begell house, Inc., New York, CD-ROM, 2006.

[14] A. Sameen, R. Verzicco, K.R. Sreenivasan, Non-Boussinesq convection at moderate Rayleigh numbers in low temperature gaseous helium, Physica Scripta T132 (2008) 014053.

[15] H.K. Versteegh, W. Malalasekera, An Introduction to Computational Fluid Dynamics – The Finite Volume Method, Longman Scientific & Technical, Harlow, England, 1995.

[16] M. Germano, U. Piomelli, P. Moin, W.H. Cabot, A dynamic subgrid-scale eddy viscosity model, Phys. Fluids A 3 (1991) 1760–1765.

[17] D.G. Barhaghi, A study of turbulent natural convection boundary layers using large-eddy simulation, Ph.D. thesis, Dept. of Applied Mechanics, Chalmers University of Technology, Göteborg, Sweden, 2007.

[18] S. Dahlström, Large eddy simulation of the flow around a high-lift airfoil, Ph.D. thesis, Dept. of Thermo and Fluid Dynamics, Chalmers University of Technology, Göteborg, Sweden, 2003.

[19] L. Davidson, S.-H. Peng, Hybrid LES-RANS: a one-equation SGS model combined with a $k-\omega$ model for predicting recirculating flows, Int. J. Numer. Methods Fluids 43 (2003) 1003–1018.

[20] R. Siegel, J. Howell, Thermal Radiation Heat Transfer, Taylor & Francis, London, England, 2002.